Available online at www.CivileJournal.org

Civil Engineering Journal

(E-ISSN: 2476-3055; ISSN: 2676-6957)

Vol. 12, No. 04, April, 2026

Investigation on the Mechanical Behavior of Passively Confined Cementitious Treated Sand

Laras Laila Lestari [1, 2], Bambang Piscesa [1*], Priyo Suprobo [1], Yudhi Lastiasih [1]

[1] *Department of Civil Engineering, Institut Teknologi Sepuluh Nopember, Surabaya 60111, Indonesia.*

[2] *Department of Civil Engineering, Institut Teknologi Adhi Tama Surabaya, Surabaya 60117, Indonesia.*

Received 28 December 2025; Revised 03 March 2026; Accepted 09 March 2026; Published 01 April 2026

Abstract

This study aims to develop a practical and accessible approach for evaluating the mechanical behavior of Cementitious Treated Sand (CTS) under passive confinement using Glass Fiber Reinforced Polymer (GFRP) wraps. A method utilizing three GFRP layer configurations was applied to investigate the confinement effect and assess the role of confining stiffness. Path-dependency was analyzed through derived confining pressure rates, and Mohr-Coulomb failure analysis was used to determine shear-strength parameters. Analysis of plastic volumetric behavior revealed that after an initial elastic state, the material dilates upon yielding—activating the confinement mechanism—before recompacting under sufficient confining pressure due to pore structure collapse. Results indicate that the proposed novel constitutive model successfully predicts both axial and lateral stress-strain responses. It accurately represents the nonlinear stress-strain relationship, the transition in volumetric behavior, and the interaction between axial and lateral strains through the proposed dilation formulation. The model incorporates a plastic dilation rate model to capture the dilation-to-compaction transition and demonstrates excellent agreement with experimental results across all confinement levels. This framework provides a reliable analytical tool for designing soil stabilization schemes using passive confinement, offering engineers a practical alternative to conventional geotechnical analysis while enhancing reproducibility, sustainability, and applicability across diverse construction projects.

Keywords: Passive Confinement; GFRP; Cementitious Treated Sand; Constitutive Model; Dilation; Confining Pressure; Path-Dependency.

1. Introduction

Granular soils, particularly poorly graded sands, are known for their susceptibility to significant deformation under load, presenting challenges in geotechnical applications. To enhance their mechanical performance, cementitious stabilization—using cement or lime additives—has been widely adopted [1, 2]. Cement-treated sands (CTS) are commonly used as fill material in embankments and as base or subbase layers in pavements [3-6]. Previous research has established that cementation increases brittleness [7, 8], shear strength [9, 10], and dilative tendency in sands [11]. However, much of this work has focused on cemented fine sands, leaving the mechanical behavior of poorly graded fine sands less explored.

Studies on cement-treated sands have emphasized the importance of density and curing conditions in governing mechanical response [12-15]. Loose, poorly graded sands represent the most critical scenario for strength and stability, as naturally deposited or uncompacted layers are frequently encountered in practice and exhibit the lowest resistance to deformation [16]. While medium and dense sands typically show higher compressive strength and stiffness under cement

* Corresponding author: piscesa@its.ac.id

https://doi.org/10.28991/CEJ-2026-012-04-03

stabilization, evaluating performance in extremely loose states provides a conservative benchmark that reflects worst-case field conditions. Another key factor is curing time, since cement-treated soils are inherently time-dependent materials [16, 17]. Strength and stiffness continue to evolve beyond the conventional 7-day curing period, with longer durations enhancing compressive strength through ongoing hydration, reducing dilation tendencies, and shifting constitutive parameters such as cohesion and modulus [18]. Despite this, much of the existing literature has focused on later-age properties [19, 20], leaving early-age performance under conservative very loose sand relatively underexplored. Addressing this gap is essential for design scenarios where rapid stabilization is required, and where the effectiveness of cement treatment must be demonstrated under the most challenging soil states.

Studies on coarser cemented materials, such as sandy gravels, have relied predominantly on triaxial compression tests to characterize stress-strain behavior [21, 22], revealing that increased cementation reduces strain at peak stress while promoting dilation and negative pore pressure after shearing [23]. Although triaxial testing remains the standard for evaluating confinement effects, there is a recognized need for complementary methods that can be employed in settings where such specialized equipment is not available [24, 25].

A promising alternative is the use of passive confinement through externally wrapped Glass Fiber Reinforced Polymer (GFRP). This approach simulates lateral pressure, effectively converting a uniaxial stress state into a triaxial one, and allows for detailed study of volumetric strain and dilation under varying stress levels without requiring a triaxial cell [26-29]. Understanding the behavior of CTS under low confining pressures is especially important for shallow geotechnical systems, where stability is influenced by surcharge loads, water table fluctuations, and adjacent constructions [30]. It should be noted, however, that GFRP confinement provides only an approximation of true triaxial conditions: lateral stresses are passively induced by the jacket rather than actively controlled, limiting stress path flexibility. Despite this limitation, the method remains practical and reproducible, offering a conservative benchmark for cement-treated sand behavior under confinement. Research on the passive confinement of CTS using GFRP—particularly on the development of constitutive models that capture its path-dependent, pressure-sensitive behavior—remains limited. Although recent studies have begun to address these issues, they focus on the use of GFRP as a soil strengthener, which is not directly relevant to the present research [31].

Hence, to address this gap, the present study investigates the mechanical behavior of CTS under passive GFRP confinement. The research examines how confinement enhances strength and modifies volumetric strain and plastic dilation rate, with the overarching aim of developing a reliable stress-strain model for design applications. Specifically, the study pursues four objectives: (1) to characterize the mechanical response of CTS confined by GFRP wraps with varying stiffness; (2) to analyze deformation behavior through the relationship between volumetric strain and plastic dilation rate; (3) to formulate a constitutive model for passively confined CTS; and (4) to validate the model by applying a variably confined concrete modeling framework to CTS under different stress conditions. Through this systematic investigation, the study aims to advance the practical understanding of CTS stabilization and contribute to more efficient geotechnical design practices.

To discuss this matter, the article is structured as follows: the research significance and contextual relevance of the study are highlighted first; the materials used and the methodology are then described; the mechanical behavior results are presented and discussed; the proposed stress–strain model based on the experimental findings is introduced; and finally, the study concludes with key insights and recommendations.

This research is significant as it addresses a critical gap in understanding the mechanical behavior of cement-treated sands (CTS) under passive confinement, particularly using Glass Fiber Reinforced Polymer (GFRP) wraps. By offering an alternative to triaxial testing, this study provides a practical and cost-effective method for evaluating the stress-strain behavior of CTS in laboratories with limited access to specialized equipment. Understanding how passive confinement influences strength, volumetric strain, and plastic dilation rate is crucial for improving stabilization techniques used in road construction, embankments, and foundation engineering. Moreover, examining CTS under low confining pressures will offer valuable insights into soil behavior in shallow-depth applications, where external factors like surcharge loads and fluctuating water tables play a vital role in stability. The findings of this research have the potential to contribute to more efficient geotechnical designs, enhancing the durability and reliability of infrastructure projects.

2. Material and Methods

The methodology employed in this study as seen in Figure 1. integrates experimental testing and constitutive modeling to evaluate the mechanical behavior of a composite material composed of loose sand, 12% cement, water, and Glass Fiber Reinforced Polymer (GFRP). Cylindrical specimens (10 × 20 cm) were prepared and wrapped with GFRP for confined triaxial strength (CTS) testing under uniaxial compression. Tensile tests were conducted to determine the GFRP's strength and Young's modulus. Experimental data—including stress-strain curves, volumetric strain behavior, and plastic dilation rates—were used to calibrate a modified Mohr-Coulomb (MC) model incorporating hardening and softening functions. The plastic potential and dilation functions were derived to refine the model, and its predictive accuracy was evaluated against experimental results to validate the proposed constitutive framework.

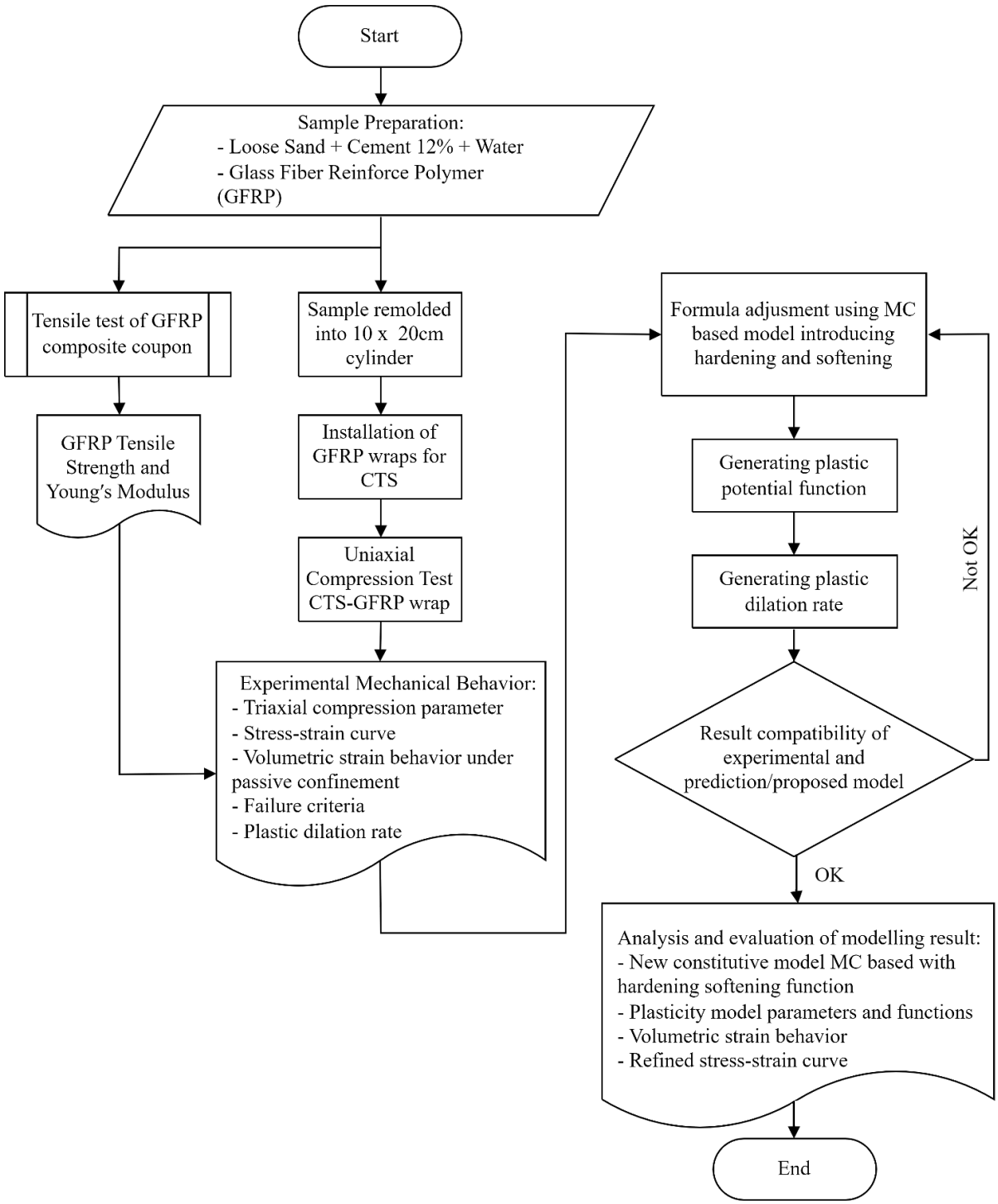

Figure 1. Research methodology

2.1. Soil and Cementing Agent Properties

The soil materials used in this research were obtained from the surface layer of soil, approximately one meter below the original ground level. These materials consist of loose sand collected from Delegan Beach, Gresik, East Java, Indonesia, including both undisturbed and disturbed samples. Sieve analysis is carried out to classify the soil sample. Figure 2 presents the gradation curves of sand material. First, the sand is sieved using No. 200 to obtain fine material, resulting in 1.56%. The remaining sand is dried and sieved with No. 4 to separate larger objects like shells, coral, and roots. All sand passes the No. 4 sieve. With fines less than five percent, the soil is classified as clean sand. The test shows a uniformity coefficient greater than four and a curvature coefficient between one and three, classifying the soil as poorly graded sand (SP). The relative density of 12.195% indicates that the sand density is extremely low, suggesting it is very loose density. Table 1 shows the sand material properties which include physical, shear strength parameter, classification, granulometry, and compaction characteristics.

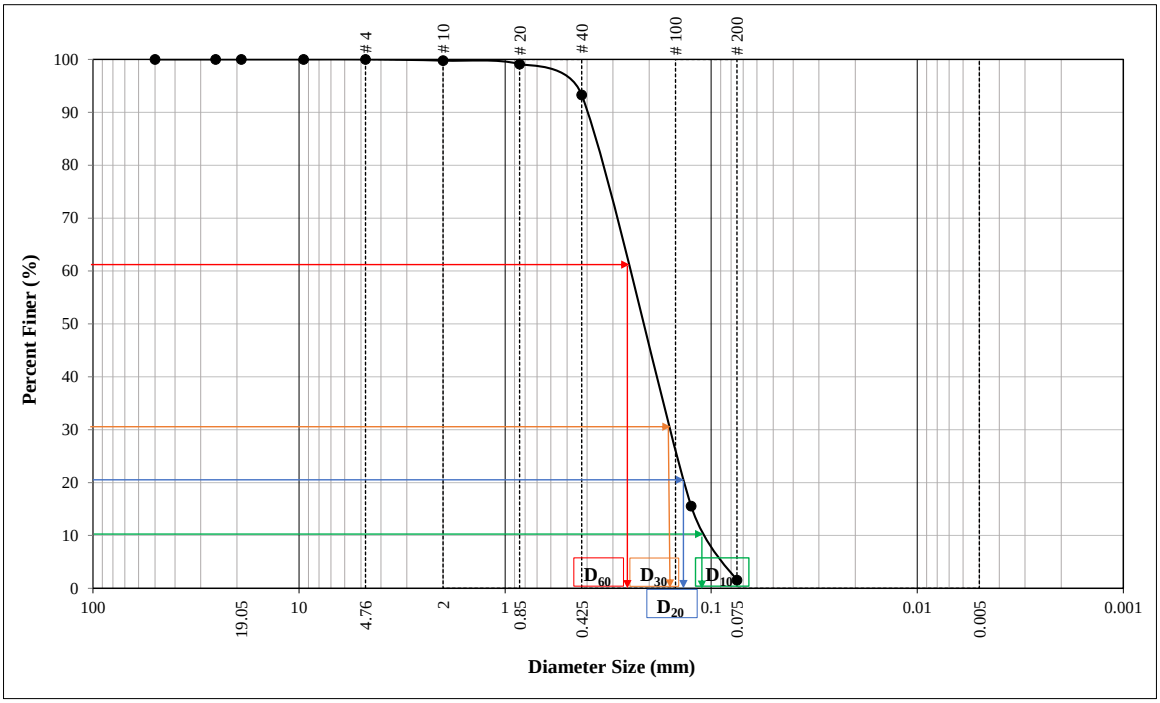

Figure 2. Gradation curve of tested sand mixture

Table 1. Sand properties

Soil Properties	Result	Test
Physical Properties		
Water Content,w (%)	7.143	ASTM D 1556
Unit Weight, γ (gr/cm^3)	1.456	ASTM D 1556
Specific Gravity, Gs	2.65	ASTM D 854-58
Relative Density, Dr (%)	12.195	ASTM D 1556
Maximum, minimum void ratios	0.92, 0.72	ASTM D4253, D4254
Shear Strength Parameter		
Internal angle friction, ϕ (°)	23.17	ASTM D 3080
Classification		
D_{60} (mm)	0.25	ASTM D 422-90
D_{30} (mm)	0.15	ASTM D 422-90
D_{10} (mm)	0.11	ASTM D 422-90
Coefficient of uniformity	2.27	ASTM D 2487
Coefficient of gradation	0.82	ASTM D 2487
Unified Classification (USCS)	SP	ASTM D 2487
AASHTO Classification	A-3	ASTM D 3283/AASHTO M145
Granulometry		
Clay (%)	0	ASTM D 422-90
Silt (%)	1.56	ASTM D 422-90
Sand (%)	98.44	ASTM D 422-90
Gravel (%)	0	ASTM D 422-90
Compaction Characteristics		
OMC, w_{opt} (%)	7.150	ASTM D 698-12
MDD, γ_{dmax} (gr/cm^3)	1.352	ASTM D 698-12
CBR (%)	7.607	ASTM D 1883

Note: MDD is the maximum dry density, and OMC is the optimum moisture content

Type I Portland cement, featuring a setting time of approximately 135 minutes, was employed as the cementing agent. The Portland cement is obtained from PT. Semen Indonesia Tbk located in Gresik, East Java, Indonesia. In this study, the cement content was fixed at 12% by weight of sand. This proportion was determined through preliminary testing in which cement contents of 6%, 8%, 10%, and 12% were evaluated. The results indicated that a cement content of 12% produced a 7-day compressive strength of 3.82 MPa, which falls within the ACI recommended strength range (2.1–4.3 MPa) for cement-treated SP-type soils [32]. Although typical field practice for SP soil-cement mixtures generally employs 7–11% cement [32], the slightly higher percentage was adopted here because it consistently satisfied the strength requirement and provided a reliable margin of safety. The choice of 12% is therefore not arbitrary but represents an optimization based on preliminary testing outcomes.

2.2. Glass-fiber Reinforced Polymer (GFRP) Properties

The glass-fiber reinforced polymer (GFRP) is fabricated by MapeWrap G Uni-Ax which featured high-strength, Uni-Directional E-Glass, Fiber Fabric. Table 2 shows the GFRP properties provided by the manufacturer. As shown in table, the design tensile strength, modulus elasticity, elongation at break and ply thickness are 297 MPa, 22,703 MPa, 1.4%, and 0.0517, respectively. The test method is based on ASTM D3039. The resin material was manufactured by CONSOL and has a type of CONSOL 88 LP. CONSOL 88 LP is a solvent-free, thixotropic, 2 component structural epoxy resin adhesive. Perfect bond for new concrete surface to old concrete.

Table 2. Glass-fiber reinforced polymer (GFRP) properties (MapeWrap G Uni-Ax0)

Properties	Average Value	Design Value[1]	ASTM Test Method
Tensile strength*	476 MPa	297 MPa	D3039
Tensile modulus*	22703 MPa	22,703 MPa	D3039
Elongation at break*	2.10%	1.40%	D3039
Ply thickness (mm)*	1.313	1.313	-

Note: * 24 sample coupons per test series according to ACI 440. Testing is in accordance with ASTM D3039.
[1] Average value minus 3 standard deviations.

2.3. Samples Preparation

2.3.1. GFRP Composite Coupon

The configuration for the GFRP laminates, which consist of the fiber and matrix, should be evaluated to obtain the correct composite properties. To produce composite materials, the volume fraction and mass fraction need to be calculated to derive the mechanical properties. Initially, the procedure involves preparing the pan and mold to the desired dimensions for the tensile test of the FRP composite. According to ASTM D3039, the dimensions for the FRP laminates are set at 25 mm × 175 mm. Subsequently, each step includes the preparation and weighing of the pan, mold, fiber, and matrix to obtain the values required for individual calculations. Illustrated in Figure 3-a are the geometric details of the tensile coupon specimen, with Figures 3-b and 3-c providing the top and side views of the specimen prepared using hand layup techniques. The technique may introduce variability due to resin accumulation and fiber distribution across plies. Although this can reduce the measured modulus in tensile coupons, the overall confinement effect is primarily governed by the jacket's tensile stiffness. To minimize inconsistencies, care was taken to maintain uniform resin application and fiber alignment during fabrication, ensuring that the jackets provided consistent passive restraint across specimens. From the sample preparation for the tensile coupon test, the thicknesses for 1, 2, and 3 plies are 1.57, 2.70, and 4.38 mm, respectively.

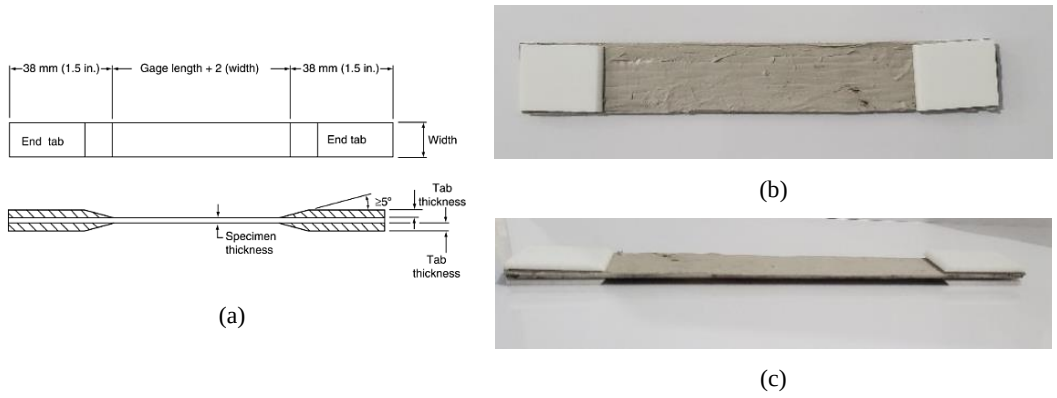

Figure 3. GFRP tensile coupon specimen

2.3.2. GFRP Confined CTS Cylinder

The specimens are prepared sand mixed with Ordinary Portland Cement (OPC) Type I per 12% weight of sand itself and remolded into the cylindrical mold of 10 × 20 cm. The specimen is cured moist, fully wrapped in plastic for 7 days at a temperature of 23±2°C. Figure 4-a and Figure 4-b show the prepared CTS specimen and fully wrapped CTS specimen under moist cured condition. The GFRP material is applied to the CTS specimen using the hand lay-up method. The epoxy adhesive is first applied to the side surface of the CTS specimen followed by wrapping the CTS specimen with GFRP sheet. Figure 4-c shows the CTS specimen wrapped with the GFRP composites. A minimum overlap with a length of ¼ × π × D, or one-fourth of the cylinder's circumference, is provided in each layer has been specified in accordance with [33]. Figure 5 shows the GFRP wrap installation and prepared overlap for each configuration.

(a) (b) (c)

Figure 4. Cement treated sand concrete cylinder: (a) CTS specimen, (b) Fully plastic wrapped CTS specimen, (c) GFRP confined CTS specimen

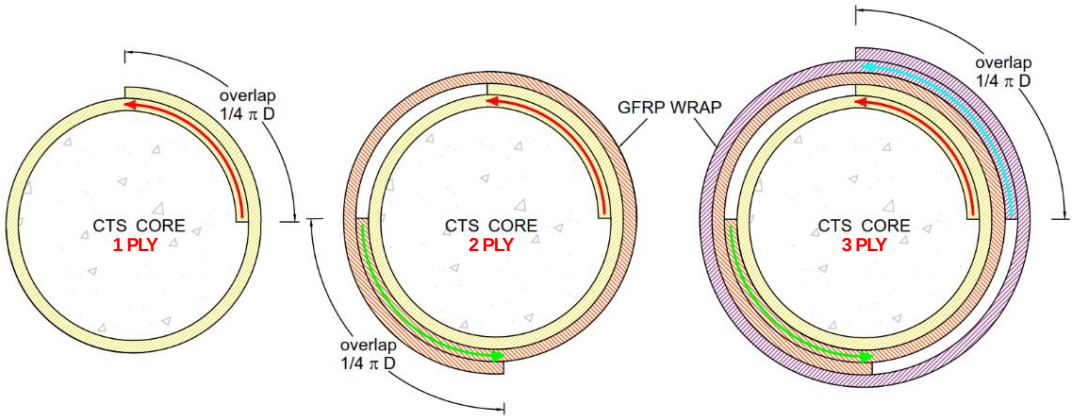

Figure 5. GFRP wrap installation and prepared overlap for each configuration

2.4. Test Set-up and Procedure

2.4.1. Tensile Coupon Test

The testing procedure for the tensile coupon specimen of the GFRP composites works by applying force applied parallel to the longitudinal direction of the fibers with dimension based on ASTM D3039 [34] and ACI, 440.2R-17 [33]. The test was performed with GFRP wraps in 1, 2, and 3 plies of laminates, which resulted in different values of tensile strength and stiffness modulus. It should be noted that the applied force and displacement was measured using the data from the testing machine (Shimadzu AGX 5kN).

2.4.2. Compression Test

Figure 6 shows the test set-up prior to compression test and positioning of the instrument to record the displacements in all directions. The applied load is measured using TML Load Cell 1 MN. Four LVDT were placed in the horizontal direction to record the lateral displacement of the samples. One LVDT in the axial direction was placed in the top loading plate. The load is applied using displacement control using the Shimadzu 500 kN universal testing machine. The instrument is attached with TDS 630 high-performance data logger. A small axial load of about 1 kN is applied as the axial seating load. The axial displacement control is applied at the rate of 1 mm/minute.

Figure 6. Loading test set-up

3. Results and Discussion

3.1. Tensile Coupon Test of the GFRP Material (ASTM D3039)

The tensile stress (s_t) and tensile strain (e_t) from the tested sample can be calculated as follows:

$$\varepsilon = \frac{\Delta L}{L_g} \text{ and } \sigma = \frac{P}{A} \quad (1)$$

where, P is the applied load, A is the coupon cross-sectional area, D_L is the extension of the coupon, and L_g is the gauge length.

Figure 7 shows the tensile stress-strain behavior for different GFRP ply numbers. Composite GFRP coupons fail suddenly and in a brittle manner [35, 36]. For one and two plies, the behavior is nearly linear, while three plies display a bilinear curve with a lower modulus until a strain of 0.022, after which it increases. Table 3 presents tensile test results: tensile strength, deformation, ultimate strain, and modulus of elasticity. Increasing plies boosts tensile strength and strain at break but reduces the elastic modulus, making the composite softer due to resin accumulation in the hand-layup process. Tensile strength rises from 125.04 MPa (1-ply) to 261.48 MPa (3-ply). Young's modulus (E_j) drops with more layers (5,136.8 MPa for 1-ply versus 2,819.4 MPa for 3-ply), indicating reduced stiffness. Deformation and strain increase, showing greater elongation before failure. The stress-strain curve likely shows a steep slope for 1-ply (higher stiffness) and a gradual slope for 3-ply (lower stiffness, higher strength, and strain). Adding GFRP layers enhances strength but reduces stiffness and increases deformability, crucial for structural applications.

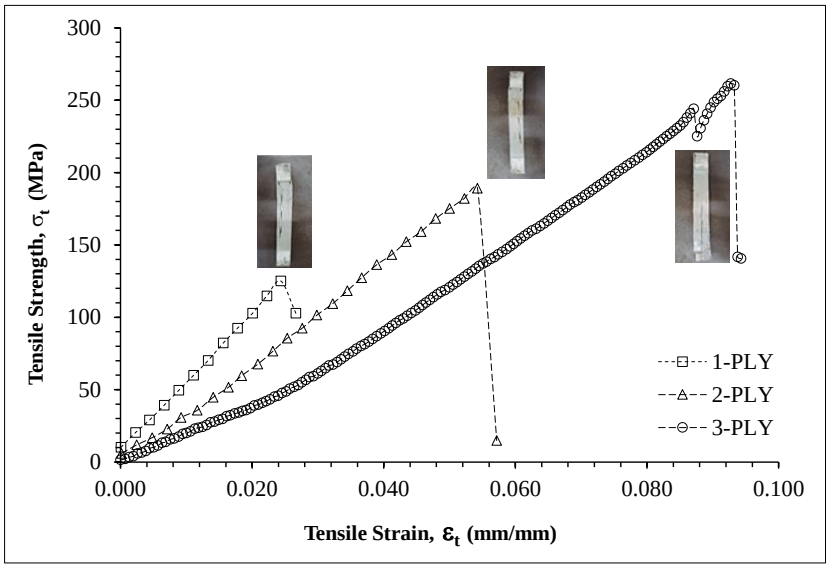

Figure 7. Tensile coupon test results in term of tensile stress and tensile strain

Table 3. Tensile coupon test results

GFRP Layer	Thickness (mm)	Tensile Strength, σ_t (MPa)	Deformation (mm)	Strain, ε_t	E_j (MPa)
1-PLY	1.57	125.04	4.26	0.024	5136.8
2-PLY	2.70	189.07	9.49	0.054	3486.6
3-PLY	4.38	261.48	16.2	0.093	2819.4

3.2. GFRP Jacket Failure Patterns

Figure 8 illustrates the deformed shape of the specimen under different phase. The phase is categorized as pre-peak, peak, post-peak, and residual stress. In the pre-peak phase, the CTS material is in an elastic condition; therefore, as the number of plies increases, the stiffness of the confined CTS also increases. Since the tensile stress of the GFRP composites with a higher number of plies is increasing, it is also expected that the peak stress prior to failure is higher as well. The post-peak phase reveals the material's ductility, with thicker laminates undergoing gradual softening due to fiber pull-out and delamination, whereas thinner laminates experience a sharper drop in stress. Residual stress highlights the remaining load-bearing capacity after failure, likely more pronounced in multi-layered specimens due to fiber bridging. This visualization underscores the trade-off between strength and ductility as the number of GFRP layers increases, providing critical insights for structural applications where damage tolerance and failure modes are key considerations. It should be noted that the point where the LVDT instrument is placed to monitor lateral deformation is not always at the location where an abrupt failure occurs. Therefore, the reading from the LVDT is limited prior to the failure of the GFRP sheets.

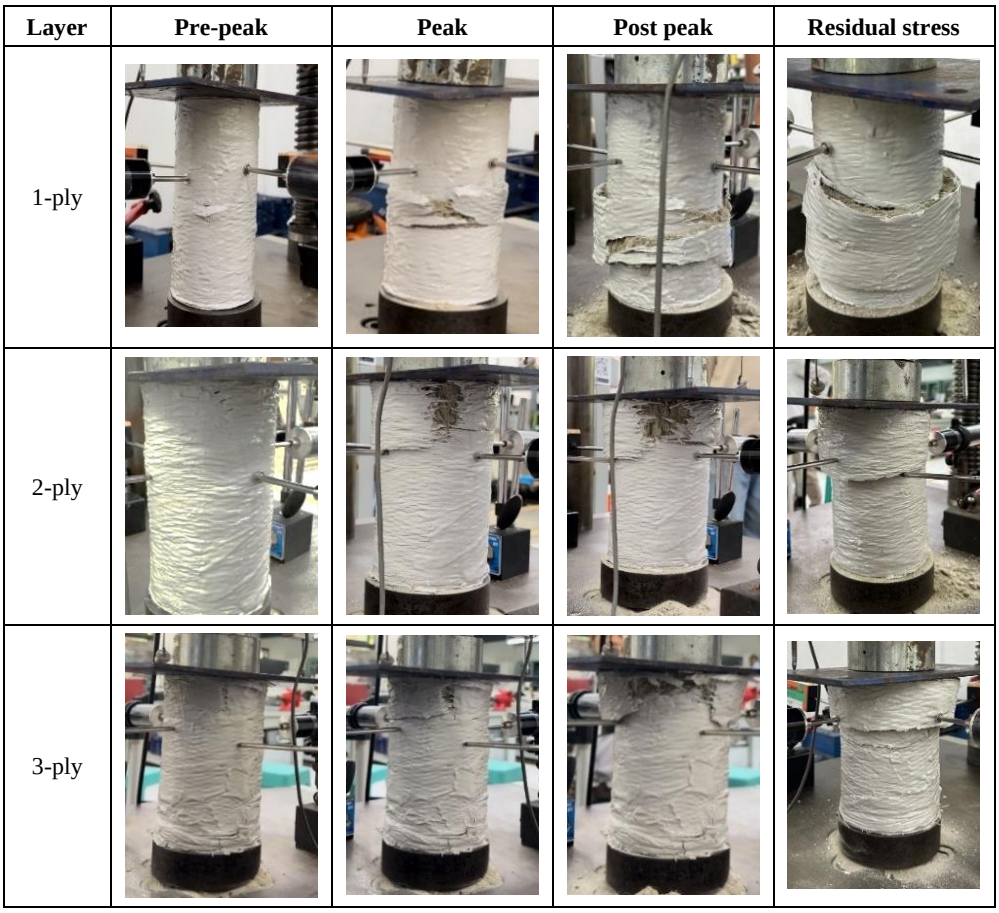

Figure 8. Deformed pattern of the specimen for each condition

3.3. Macro-Mechanical Response of Confined CTS

The axial stress and strain curves for the CTS specimen—comprising one unconfined CTS specimen and three GFRP confined CTS specimens—are presented in Figure 9. Axial stress is calculated by dividing the applied axial load by the cross-sectional area of the concrete cylinder. Axial strain is determined by dividing the axial shortening, measured using the LVDT, by the total length of the undeformed specimen. From the test, it can be observed that the unconfined CTS compressive strength (s_{3u}) is 3.602 MPa. The pre-peak behavior of all specimens is nearly linear, reflecting elastic deformation; however, the slopes vary, indicating differences in stiffness. A typical and almost linear hardening axial

stress-strain behavior was observed for GFRP confined CTS specimens. Table 4 shows the maximum value of the confining pressure prior to failure (f_r), axial stress at peak (s_{cc}), axial strain at peak stress (e_{cc}), and lateral strain at peak stress (e_{lat}). The confining pressure (f_r) is estimated using the compatibility equation between the concrete core and the confining devices which is [37]:

$$f_r = \varepsilon_{lat} E_L = \varepsilon_{lat} \left[\frac{2ntE_j}{D}\right] \quad (2)$$

where n is the number of piles, t is the thickness of one ply FRP, E_j is the elastic modulus of the jacket, E_L is the lateral modulus of the confining device, and D is the diameter of the confined concrete core. From the Table 4, the lateral strain (e_{lat}) in concrete prior to failure is significantly lower than the rupturing strain (e_{rup}) of the FRP material obtained from the tensile coupon test. The hoop stress (s_q) acting on the FRP material is also less than the tensile strength (s_t) derived from the tensile coupon test. Furthermore, as the thickness increases from one to two plies of GFRP wrap, the hoop stress on the sheet decreases due to the reduced jacket modulus. However, the confining pressure (f_r) calculated using Equation 2 increases with the number of plies.

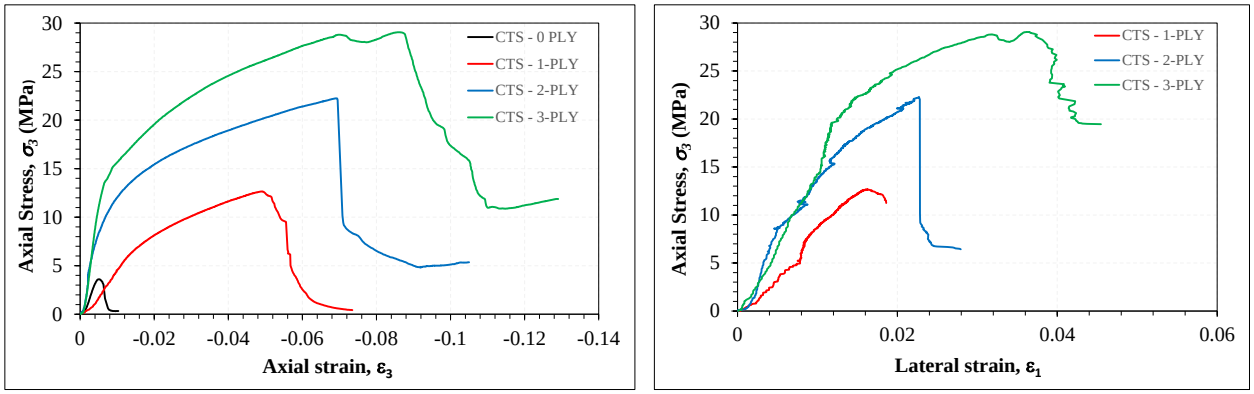

Figure 9. Axial and lateral stress-strain curves for GFRP confined CTS specimens

Table 4. Maximum values for the confining pressure, axial stress, axial strain, and lateral strain

n_{ply}	σ_{cc} (MPa)	E_L (MPa)	f_r (MPa)	σ_θ (MPa)	σ_t (MPa)	$\varepsilon_{cc\ axial}$	ε_{lat}	ε_{rup}
1	12.65	161.29	2.58	82.18	125.04	-0.049	0.016	0.024
2	22.25	188.24	4.14	76.69	189.07	-0.069	0.022	0.054
3	29.05	246.94	8.89	101.48	261.48	-0.086	0.036	0.093

The volumetric strain shows the measurement of change in volume relative to the original volume of material (DV/V_0) [38]. The volumetric strain of the tested specimen holds an important meaning where in the case of CTS material, once the material is no longer elastic, the volume would expand and when the confining pressure is sufficiently large, the material would compress leading to a negative rate of the volumetric strain. The total volumetric strain (e_v) can be computed by summing all the normal strain in the principal direction (e_1, e_2, = e_{lat} and e_3 = e_{ax}) and is:

$$\varepsilon_v = \varepsilon_1 + \varepsilon_2 + \varepsilon_3 = 2\varepsilon_{lat} + \varepsilon_{3ax} \quad (3)$$

The elastic volumetric strain (e_{ve}) can be easily calculated by using the Hook's law and therefore the plastic volumetric strain can be obtained by subtracting the elastic volumetric strain from the total volumetric strain (e_{vp}). Elastic volumetric strain refers to the temporary change in volume that occurs when a material is subjected to a load within its elastic limit, enabling it to return to its original shape once the load is removed. In contrast, plastic volumetric strain indicates the permanent change in volume that occurs when a material is subjected to a load exceeding its elastic limit, leading to irreversible deformation even after the load is removed [39]. Figure 10 shows the volumetric strain behavior of the tested GFRP confined CTS material. The figures show total volumetric strain as a solid line and elastic volumetric strain as a long-dashed line. Elastic strain is the sum of its principal components, derived via Hooke's law for specific stresses over time. For the GFRP confined specimen with linear hardening, the elastic volumetric strain continuously increases until the confining material fails. Initially, the volumetric strain compacts due to the material's elastic behavior, then begins to dilate when transitioning out of the elastic range or upon damage. The volumetric strain reaches zero when the elastic volumetric strain equals the plastic volumetric strain. These zero volumetric strains signify the peak condition for actively confined concrete [37, 40]. Below zero volumetric strain, the material starts to soften. In the figure, the plastic volumetric strain at peak, when the volumetric strain is zero, equals the negative of the elastic volumetric strain at peak.

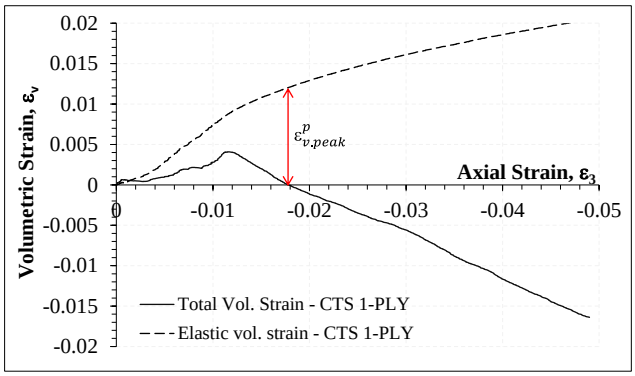

(a) One-ply

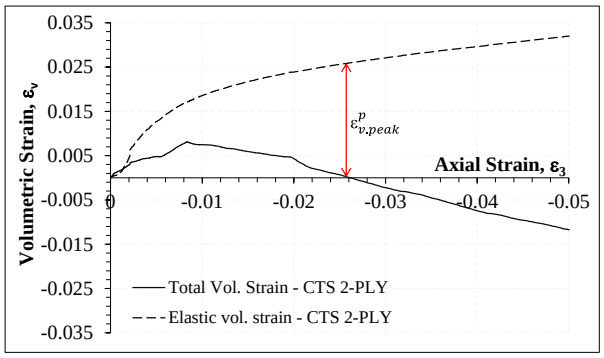

(b) Two-ply

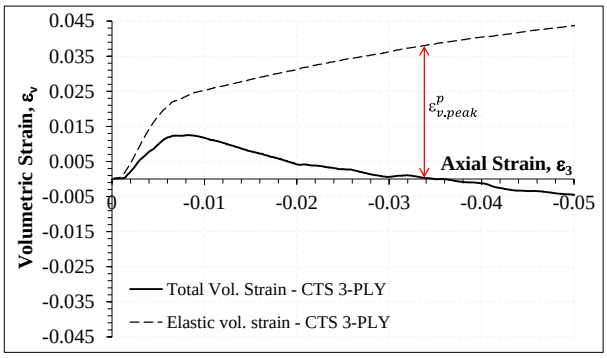

(c) Three-ply

Figure 10. Volumetric strain behavior of the GFRP wrapped CTS specimen

The axial stress associated with each axial strain provides a comprehensive history of the evolution of the loading surface. At the onset of localized cracking or damage, the loading surface transitions from the initial state to the failure surface (peak loading surface) as the loading and damage progress. The parameter that governs the loading surface is often expressed in terms of irreversible strain, referred to here as plastic strain. For a quasi-brittle, pressure-sensitive, and path-dependent material, plastic volumetric strain is preferred as the driving parameter for the evolution of the loading surface. As discussed previously, it is established that when the volumetric strain is zero, the corresponding axial stress is at peak stress, as seen in the active confinement scheme. Thus, the condition of zero volumetric strain signifies that the stresses are positioned on the failure surface (peak loading surface), allowing for the back calculation of the relevant confining pressure using the compatibility equation.

From the tests carried out in this paper, three confinement levels correspond to different numbers of plies of the GFRP wrap. For each confinement level, there exists a point where the volumetric strain is zero. These points are used to determine the angle of inclination of the failure surface, as well as the initial cohesive value of the CTS material. Figure 11 illustrates how to obtain the axial stress corresponding to the zero volumetric strain conditions. The corresponding axial stress is identified by locating the axial strain at which the volumetric strain is zero in the axial stress-strain curves. Once the axial stress point is identified, the corresponding lateral strain is obtained by examining the same axial stress in the axial stress versus lateral strain curves. Lateral strains obtained have smaller values than axial strain and are thus more prone to noise, but averaging multiple LVDTs with filtering and calibration minimized this effect.

Consequently, the zero volumetric strain point was determined from smoothed data, ensuring reliable identification of peak stress. The confining pressure can then be calculated using Equation 2 with the lateral strain input obtained from this procedure. In the figure, the transitions from compaction to dilation are captured. The volumetric strain curves show that the onset of dilation (zero volumetric strain) occurs progressively later with increasing ply number, at axial strains of approximately −0.017, −0.025, and −0.036 for 1-, 2-, and 3-ply specimens, respectively. Corresponding axial stresses and lateral strains at this state are 7.4 MPa/0.009, 16.6 MPa/0.013, and 23.7 MPa/0.018, all occurring before peak strength. This comparison demonstrates that confined CTS continues to accumulate substantial deformation and dilatancy beyond the critical state, with higher confinement narrowing the stress gap between zero volumetric strain and peak strength while amplifying strain development, thereby enhancing ductility and volumetric expansion prior to failure.

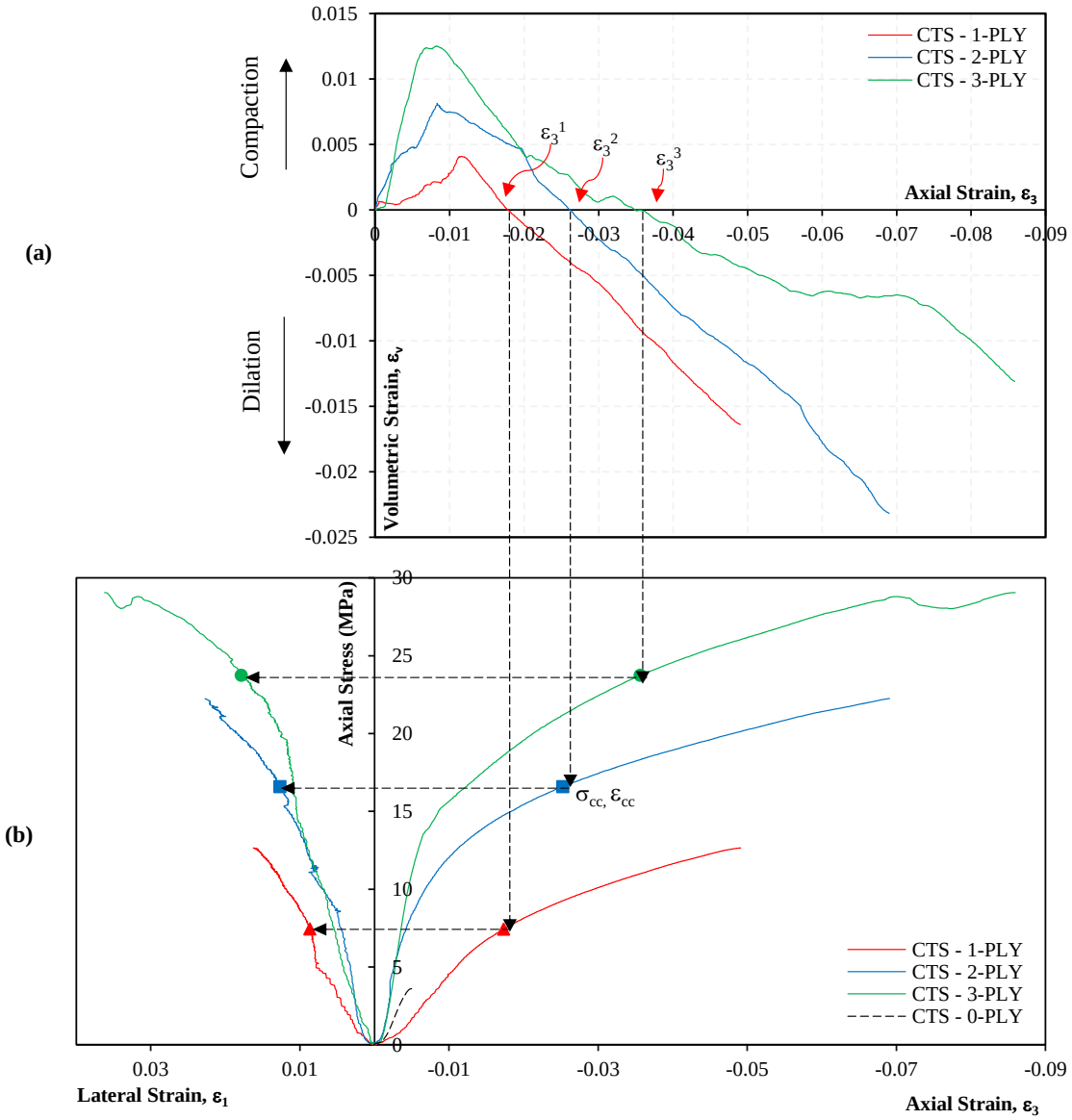

Figure 11. Relationship between the volumetric strain and axial stress versus axial strain for different ply configurations to determine the axial stress, axial strain, and lateral strain which correspond to zero volumetric strain

The extracted data of axial stress, axial strain, and confining pressure at zero volumetric strain is shown in Table 5. Figure 12-a and Figure 12-b displays the response of axial stress and strain as functions of confining pressure ratio corresponding to zero volumetric strain. In Figure 12-a, the axial strain increases with increasing confining pressure, indicating enhanced material ductility. Similarly, Figure 12-b illustrates that axial stress increases with confining pressure, which is an expected behavior. The formula to forecast the axial strain and axial stress are prepared using linear forecasting method and are:

$$\varepsilon_{3cc} = 0.005 + 0.0267\frac{f_r}{\sigma_{3u}} \quad (4)$$

$$\sigma_{3cc} = \left(\sigma_{3u} + 16.66\frac{f_r}{\sigma_{3u}}\right) \text{MPa} \quad (5)$$

where e_{3cc} and σ_{3cc} are the forecast of axial strain and stress respectively, f_r is confining pressure, σ_{3u} is the uniaxial compressive strength of the CTS material.

Table 5. Axial stress, axial strain, and confining pressure at zero volumetric strain

n_{ply}	σ_{cc} (MPa)	E_L (MPa)	f_r (MPa)	σ_θ (MPa)	$\varepsilon_{cc\ axial}$	ε_{lat}
1	7.43	161.29	1.45	46.32	-0.0173	0.009
2	16.58	188.24	2.45	45.32	-0.0253	0.013
3	23.74	246.94	4.45	50.72	-0.0357	0.018

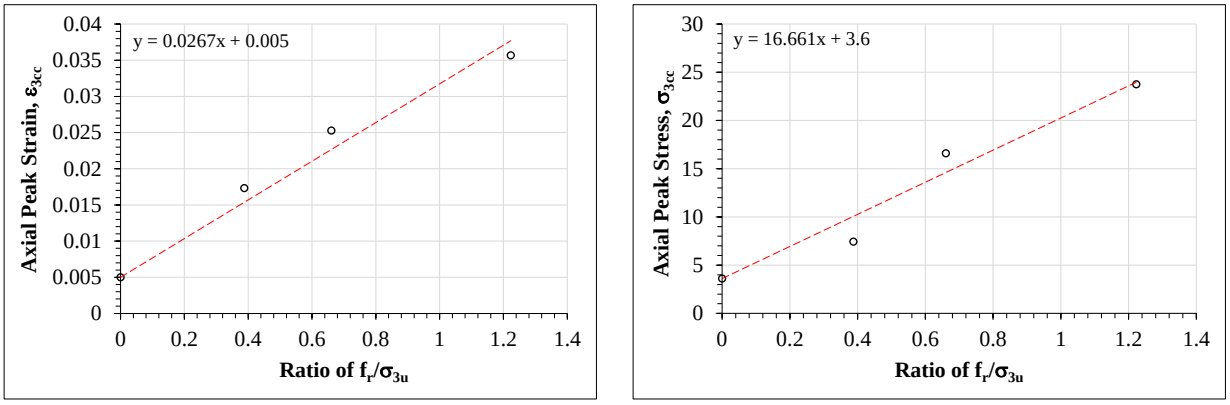

(a) (b)

Figure 12. Confining Pressure Relationship (a) Confining pressure vs Axial strain (b) Peak stress vs confining pressure

3.4. Shear Strength and Pressure-Dependent Friction

The shear strength of the CTS specimen can be predicted using at least three triaxial test of the CTS specimen with varying confining pressure. Figure 13 presents the graphical representation of the Mohr-Coulomb circles derived from the data in Tables 4 and 5. The data in Table 4 pertains to the ultimate condition of the GFRP confined CTS specimen, where the loading surface has experienced softening in comparison to the peak loading or failure surface. In contrast, Table 5 contains data corresponding to the peak loading surface, described under conditions of zero volumetric strain. The peak shear stress for each circle can be determined to evaluate the material's shear strength through the application of linear curve fitting. It is well-established that the intersection of Mohr's circles with the failure envelope signifies the stress conditions leading to material failure [38, 41-43]. From the linear forecasting, the friction angle (23.9 degrees) of the failure surface (from the data corresponding to the zero volumetric strain) was higher compared to the friction angle (23.9 degrees) of the softened loading surface (from the final data at the onset of GFRP wrap failure). This means that the friction angle was reduced as the material become more damaged. From the linear forecasting, it was found that the shear stress of the CTS material with zero normal stress is 2.1 MPa and the internal friction angle is 23.9 degrees (using the peak recorded data). On the other hand, by using the data which related to the zero-volumetric strain, the shear stress is 0.2 MPa with the internal friction angle of 34 degrees.

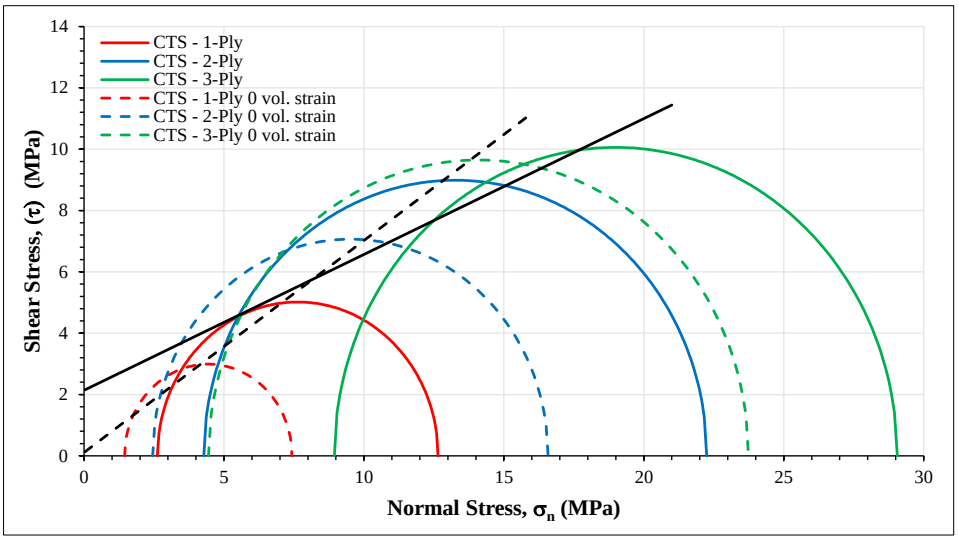

Figure 13. Mohr-Coulomb circle of the GFRP confined CTS specimen

3.5. Evolution of the Plastic Dilation Rate

Under passive confinement, the plastic dilation rate response should exhibit plastic volumetric compaction when the elastic confining device generates very high confining pressure. This phenomenon is observed in concrete confined with FRP of very high stiffness. A critical benchmark for the plastic dilation rate is that it should remain below the incompressible limit, specifically $|\beta| \leq 0.5$, when elastic confining devices produce very high confining pressure [44].

Figure 14 illustrates the predicted plastic dilation rate based on Equation 8. At the initiation of plastic flow, the plastic dilation rate begins at zero and subsequently reaches the minimum plastic dilation rate. The initial plastic compaction, indicated by the shaded region in Figure 14, occurs when the value of plastic dilation rate is less than 0.5. The area below -0.5 shows as a plastic volumetric compaction. The behavior of the 1-ply specimen exhibits initial plastic

compaction, followed by dilation, and subsequent compaction. The 2-ply specimen demonstrates a similar pattern; however, it transitions to dilation earlier due to a higher ratio of confining pressure to the strength of CTS. The 3-ply GFRP specimen displays a distinct behavior, characterized by a larger ratio of confining pressure to the strength of CTS and the highest lateral modulus. It exhibits a leaner structure, and its position is very close to 0.5, indicating minimal dilation and a dominance in plastic volumetric compaction. This observation is consistent with [44], which states that if the confining pressure is sufficiently high, plastic volumetric compaction will occur under the same conditions as initial plastic compaction. Furthermore, for very stiff confining devices, compaction can occur from the beginning of plastic flow.

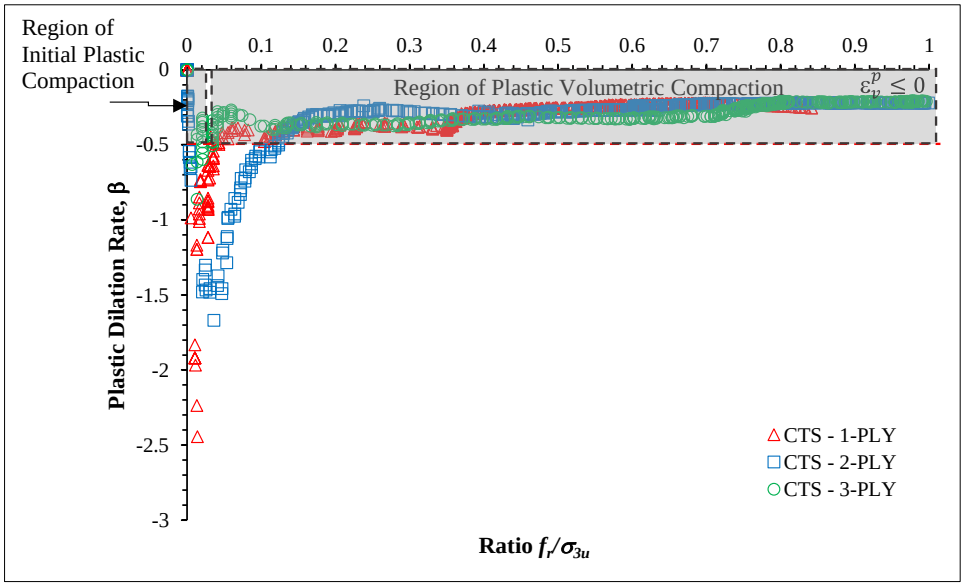

Figure 14. Plastic Dilation Rate Characteristic for Confined CTS

4. Proposed Stress-Strain Model

4.1. Failure Surface and the Hardening Functions

The constitutive model for passively confined CTS is formulated within a plasticity framework. The yield and failure behavior is governed by a pressure-sensitive loading surface based on the Mohr-Coulomb criterion, expressed in terms of stress invariants to facilitate numerical implementation. This surface evolves through hardening and softening functions, allowing the model to capture the progressive development of strength up to a peak and the subsequent post-peak degradation. Figure 15 shows the Mohr-Coulomb failure surface in both the meridian plane (q-0º) and p-Plane. In the meridian plane, there exist compressive and tensile meridian. In many cases, for quasi-brittle material (concrete, rocks, hardened-soil), the tensile meridian has lower friction angle compared to the compressive meridian. Therefore, the deviatoric trace for uniaxial case in tensile meridian is smaller and therefore the tensile friction angle (f_t) is smaller than the compressive friction angle (f_c). In the case of uniform confinement, the lode angle (θ) is equal to sixty-degree and therefore only the compressive meridian is active.

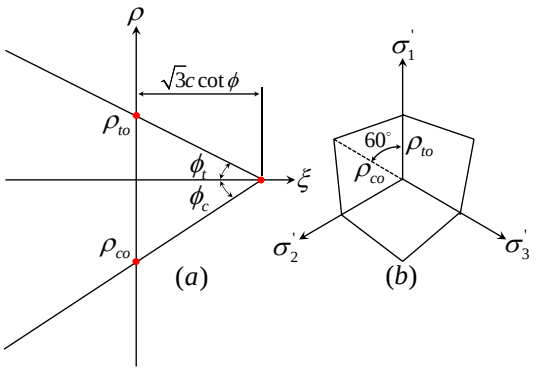

Figure 15. . Mohr-Coulomb failure surface: (a) Meridian Plane q-0º and (b) p-Plane

The loading surface for the confined CTS is using the Mohr-Coulomb failure surface with hardening (q_h) and softening functions (q_s). The peak loading surface occurred when the value for the hardening and softening functions equal to unity. The Mohr-Coulomb criterion in terms of variable ξ, ρ, θ can be written as:

$$f(\xi,\rho,\theta) = \sqrt{2}\xi\ sin\ \phi_1 + \sqrt{3}\rho\ sin\left(\theta + \frac{\pi}{3}\right) + \rho\ cos\left(\theta + \frac{\pi}{3}\right) sin\ \phi_1 - \sqrt{6}c\ cos\ \phi_1\ q_h q_s = 0 \quad (6)$$

here variable ξ is hydrostatic axis, ρ is deviatoric radius, and θ is lode angle in the terms of invariants (I_1, J_2, and J_3). The material strength parameters are the cohesion c and the compressive friction angle f_1. The terms q_h and q_s are the hardening and softening functions, respectively, which modulate the size of the loading surface.

In Equation 6, f_1 is the friction angle in compressive cases where as previously discussed in Section 4.4, it was observed that the friction angle was reduced as the confining pressure and damage in the material increases. The friction angle of the failure surface was governed by the confining pressure (f_r), the cohesive (c), the confining device stiffness in terms of the lateral modulus (E_L) of the confining device, and the uniaxial compressive strength of the material (σ_{3u}). The proposed expression for the friction angle is as follows:

$$\phi_x = 17 + 17(1 - exp(-0.0536 \times max(E_L - 161,0))) \quad (7)$$

$$\left[\sqrt{J_2}\ sin\left(\theta + \frac{\pi}{3}\right) + \frac{\sqrt{J_2}}{\sqrt{3}} cos\left(\theta + \frac{\pi}{3}\right) sin\ \phi\right] \approx A\sqrt{J_2}(B - sin\ \phi) \quad (8)$$

$$\sigma_{3u} = \frac{2c\ cos\ \phi_1}{1 - sin\ \phi_1} \quad (9)$$

$$\sigma_{3u} = \frac{2c\ cos\ \phi_1}{1 - sin\ \phi_1} \quad (10)$$

As shown in Equation 7, the initial friction angle was reduced as the confining pressure increases. This phenomenon is caused by the reduced confining effect to the material strength enhancement. Furthermore, in Equation 8, it is clear that any confining device with the lateral modulus value less than 161 MPa is considered to have no effects on the initial friction angle value for the cementitious treated sand.

In Equation 6, the hardening functions are expressed in terms of the hardening function (q_h) and softening function (q_s). The hardening function (q_h) is adopted from [45] and is:

$$q_{\square}(k) = k_0 + (1 - k_0)\sqrt{1 - (1 - k)^2} \quad (11)$$

where k_0 is the base hardening parameter, k is the hardening parameter which is a function of the accumulated axial plastic strain $\left(\varepsilon_3^p\right)$ divided with the axial plastic strain at peak $\left(\varepsilon_{3,peak}^p\right)$. In Equation 11, k_0 is set to 0.4. The expression for the hardening parameter is:

$$k = \frac{\varepsilon_3^p}{\varepsilon_{3,peak}^p} \quad (12)$$

In Equation 12, the axial plastic strain at peak $\left(\varepsilon_{3,peak}^p\right)$ can be calculated by subtracting the axial strain at peak (ε_{3cc}) in Equation 4 with the elastic axial strain at peak $\left(\varepsilon_{3,peak}^e = \sigma_{3u}/E_{cts}\right)$. On the other hand, the softening function is adopted from [37, 46] and is:

$$q_s = q_{st}^{\alpha};\ \alpha = \left(\frac{k-1}{k_i - 1}\right)^2 \quad (13)$$

where k_i is the hardening parameter at the inflection point of the softening curve and is:

$$k_i = \frac{\varepsilon_{3,j}^p}{\varepsilon_{3,peak}^p} \quad (14)$$

where, $(\varepsilon_{3,j}^p)$ is the axial strain at the inflection point of the softening curve and is taken as two times ε_{3cc}. Furthermore, in Equation 13, q_{si} is the hardening value at the inflection point when the CTS material softens and the value is set to 0.8.

The numerical incremental method is driven by the axial strain (e_{3cc}). However, the hardening parameter is defined in terms of the plastic axial strain. Therefore, evaluation of the trial stress should be done incrementally. The trial stress is evaluated using the failure surface as shown in Equation 6. If the trial stress lies outside the surface of failure, the trial stress must be corrected. Please refer to Piscesa et al. [29] for the return mapping algorithm. In Piscesa et al. [29], the return mapping algorithm is using the secant-method and regula-false method.

4.2. Plastic Potential Function

The plastic potential function of the proposed model is taken to have similar form with the failure surface, however, the internal friction angle (f_2) is not similar and also degraded to simulate the reduction in the dilatant behavior once the

CTS is damaged and finally compacted which shows a value of the internal friction angle less than zero (negative). The expression of the plastic potential function is done by rewriting Equation 6, substituting f_1 with f_2, and eliminating the hardening functions (q_h and q_s), becomes:

$$g(\xi,\rho,\theta) = \sqrt{2}\xi \sin\phi_2 + \sqrt{3}\rho \sin\left(\theta+\frac{\pi}{3}\right) + \rho\cos\left(\theta+\frac{\pi}{3}\right)\sin\phi_2 - \sqrt{6}c\cos\phi_2 = 0 \quad (15)$$

The internal friction angle for the plastic potential function which considers the evolution of the plastic dilation rate of the CTS material from dilation when the confining pressure is low and compaction when the confining pressure is high can be written as:

$$\phi_2 = max\left(60-(60+40)\tanh\left(a\left(\frac{f_r}{\sigma_{3u}}\right),-\frac{E_L}{36}\right)\frac{\pi}{180}\right) \quad (16)$$

4.3. Plastic-Dilation Rate (β)

The plastic dilation rate of the model can be derived by taking the ratio of the plastic strain in the lateral direction with respect to the plastic strain in the axial direction. Since the plastic multiplier (l) is present in both directions, the plastic dilation rate formulation can be simplified by only consider the differentiation of the plastic potential function with is respected stresses and therefore:

$$\frac{\partial g}{\partial\sigma_i} = \frac{\partial}{\partial\sigma_i}\left(\frac{1}{3}I_1\sin\phi_2\right) + \frac{\partial}{\partial\sigma_i}\left(\sqrt{J_2}\sin\left(\theta+\frac{\pi}{3}\right)\right) + \frac{\partial}{\partial\sigma_i}\left(\frac{\sqrt{J_2}}{\sqrt{3}}\cos\left(\theta+\frac{\pi}{3}\right)\sin\phi_2\right) - \frac{\partial}{\partial\sigma_i}(c\cos\phi_2) = 0 \quad (17)$$

$$g_1 = \frac{1}{3}\sin\phi_2 + \frac{(\sigma_1-\sigma_3)}{6{J_2}^{0.5}}\sin\left(\theta+\frac{\pi}{3}\right) + \frac{(\sigma_1-\sigma_3)}{6\sqrt{3}{J_2}^{0.5}}\cos\left(\theta+\frac{\pi}{3}\right)\sin\phi_2 \quad (18)$$

$$g_3 = \frac{1}{3}\sin\phi_2 + \frac{(\sigma_3-\sigma_1)}{3{J_2}^{0.5}}\sin\left(\theta+\frac{\pi}{3}\right) + \frac{(\sigma_3-\sigma_1)}{3\sqrt{3}{J_2}^{0.5}}\cos\left(\theta+\frac{\pi}{3}\right)\sin\phi_2 \quad (19)$$

$$\beta = \frac{g_1}{g_3}. \quad (20)$$

The performance of the proposed plastic dilation rate formulation is evaluated by inputting the confining pressure ratio (f_r/s_{3u}) and f_2 into Equation 20. Since in Equation 16, the internal friction angle is function of both the normalized confining pressure and the lateral modulus of the confining device, the plastic dilation rate curves for each different of ply is also not similar. Figure 16 illustrates the prediction of the plastic dilation rate (β) as a function of the confining pressure ratio (f_r/s_{3u}), incorporating both experimental data and the proposed model. The model prediction, shown as a red dashed curve, is derived from the ratio of uniaxial and triaxial flow rule formulation. The CTS specimen of 1-PLY and 2-PLY, showing a gradual approach to compaction and clearer separation between the initial dilation regime and the compaction regime. However, for the 3-PLY configuration, which exhibits higher stiffness, the compaction behavior emerges earlier. The agreement between the experimental data and the model across all ply configurations reinforces the validity of the proposed dilation formulation and its sensitivity to confinement effects.

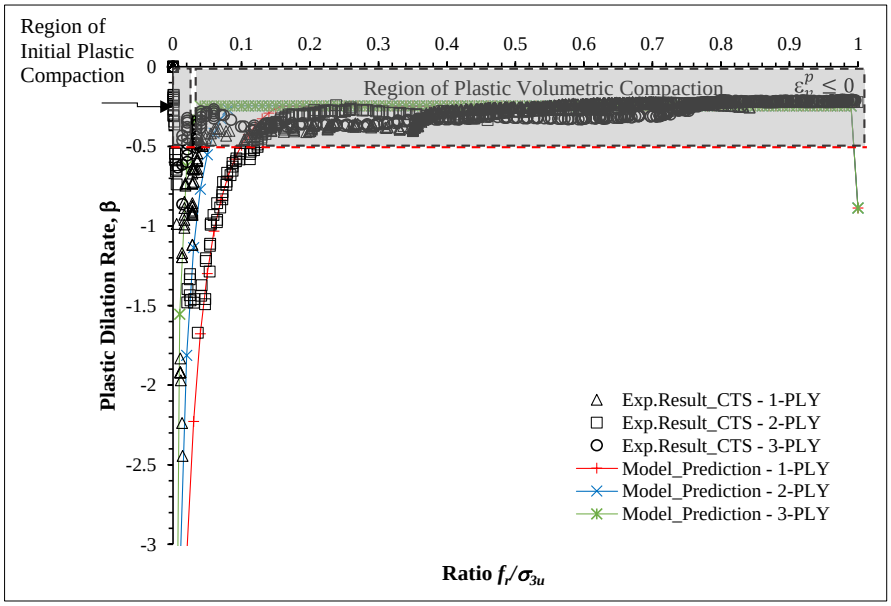

Figure 16. Plastic dilation rate prediction compared with the test results

4.4. Performance Evaluation of the Proposed Constitutive Model

The predictive capability of the proposed stress-strain model was assessed by comparing its simulations with experimental results for CTS specimens confined with varying numbers of GFRP layers (1-ply, 2-ply, and 3-ply). Figure 17 presents the comparative axial stress–strain and lateral strain responses.

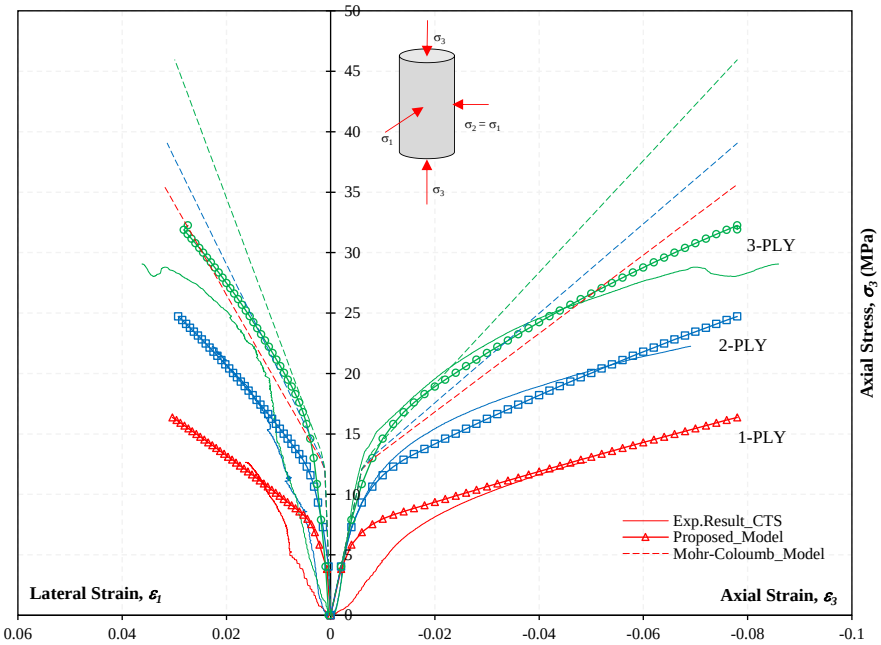

Figure 17. Proposed Model Comparison with Experimental Results (Axial Stress vs Axial Strain and Lateral Strain)

4.4.1. Axial Stress-Strain Response

The experimental data demonstrates a clear confinement effect: peak axial stress increases progressively with additional GFRP layers. The 3-ply configuration achieved the highest peak stress (29.055 MPa), followed by the 2-ply (22.25 MPa) and 1-ply (12.65 MPa) specimens. The proposed model exhibits excellent agreement with experimental curves across all configurations, accurately capturing the initial linear elastic response, the nonlinear hardening phase leading to peak stress, the increased ductility with higher confinement levels. Notably, the model successfully replicates the increased stiffness and peak stress enhancement observed in multi-ply specimens, confirming its ability to incorporate confinement-induced anisotropy and strain-dependent stiffness degradation.

However, comparison with the basic Mohr–Coulomb model (represented by the dashed curves) shows an increase in peak stress with added confinement. Nevertheless, the model substantially overestimates the experimental results for the 1‑ ply, 2‑ ply, and 3‑ ply cases by 181.7%, 75.5%, and 58.2%, respectively. It indicates that the basic Mohr–Coulomb model substantially overpredicts peak strength and does not provide a realistic prediction of behavior. The basic Mohr–Coulomb model treats post‑ yield behavior as perfectly plastic, so once the yield surface is reached the material is assumed to deform at a constant stress; this idealization neglects common responses such as strain hardening or strain softening. Additionally, the basic Mohr–Coulomb model does not explicitly include plastic dilatancy—the volumetric expansion that can accompany shear—which alters the stress path and can affect failure mechanism [47].

4.4.2. Lateral Strain Prediction

The model's prediction of lateral strain evolution shows generally good correlation with experimental measurements, though subtle deviations exist. For the 1-ply configuration, the model slightly overestimates lateral expansion at higher axial strains. Nevertheless, the overall trends remain well-captured, particularly for 2-ply and 3-ply specimens where confinement is more substantial. The model's formulation of lateral strain evolution—governed by the variable plastic dilation rate described in Equation 23—effectively represents the transition from dilative to compressive volumetric behavior as confining pressure increases. While the proposed model provides values closer to the experimental results, the basic Mohr–Coulomb model overestimates lateral strain by 97.5% for the 1‑ ply case—the largest error observed—and by 38.1% for the 2‑ ply case but underestimates it by 17.4% for the 3‑ ply case. These discrepancies indicate that the basic Mohr–Coulomb formulation lacks mechanisms to account for volumetric response (dilatancy), anisotropy, and damage evolution; as a result, it tends to predict excessive lateral expansion at low confinement and fails to capture the excessive lateral response of the 3‑ ply specimen.

Based on that comparison, the proposed model—an extension of the Mohr–Coulomb criterion incorporating hardening and softening functions—can satisfactorily capture the nonlinear behavior of confined CTS. It also accounts for the evolving values of cohesion and friction with plastic strain, which reduce stiffness and provide strain‑localization control, thereby allowing the model to reproduce both pre‑peak and post‑peak hardening while emphasizing the influence of plastic dilatancy, and thus achieving a closer match to the experimental results.

5. Conclusion

This study has demonstrated that passive confinement using Glass Fiber Reinforced Polymer (GFRP) wraps significantly enhances the mechanical performance of cement-treated sand (CTS). Experimental results revealed clear improvements in strength and ductility, with peak axial stress increasing as the number and stiffness of GFRP layers rises. The confinement mechanism was observed to activate after initial dilation, supplying lateral restraint that restricted volumetric expansion and induced re-compaction. This transition underscores the pressure-dependent response of CTS, where sufficient confinement can shift the material from a dilative to a compactant state. The developed constitutive model successfully captured these essential features, reproducing the nonlinear stress–strain relationship, the volumetric transition, and the coupling between axial and lateral strains through the proposed dilation formulation. Validation was achieved by applying a variably confined concrete modeling framework to CTS under different stress conditions, with predictions aligning closely to experimental data, particularly at higher confinement levels. This confirms the model's reliability as an analytical tool and highlights its potential as a practical alternative to conventional triaxial testing in contexts where specialized equipment is unavailable.

From a practical standpoint, this study offers valuable insights into geotechnical soil stabilization. GFRP-wrapped cement-treated sand (CTS) emerges as a viable and accessible technique for enhancing the performance of road bases, embankment fills, and shallow foundations, particularly under low confining pressures typical of near-surface systems. The findings contribute to more economical and sustainable design approaches, enabling engineers to better predict and improve the behavior of cemented soils in both new construction and rehabilitation projects. Future research should explore diverse soil types, cement contents, and curing durations, while also assessing long-term durability under cyclic or dynamic loading. Refining the constitutive model to incorporate interface effects and complex loading paths will further strengthen its predictive capability.

6. Declarations

6.1. Author Contributions

Conceptualization, L.L.L. and B.P.; methodology, L.L.L.; software, B.P.; validation, L.L.L., B.P., P.S., and Y.L.; formal analysis, L.L.L. and B.P.; investigation, L.L.L.; resources, L.L.L. and B.P.; data curation, L.L.L. and B.P.; writing—original draft preparation, L.L.L. and B.P.; writing—review and editing, L.L.L. and B.P.; visualization, L.L.L. and B.P.; supervision, B.P., P.S., and Y.L.; project administration, L.L.L.; funding acquisition, L.L.L and B.P. All authors have read and agreed to the published version of the manuscript.

6.2. Data Availability Statement

The data presented in this study are available in the article.

6.3. Funding and Acknowledgments

This work is made possible by a graduate scholarship awarded to the first author by the Indonesian Education Scholarship (BPI), the Center for Higher Education Funding and Assessment (PPAPT) of the Indonesian Ministry of Higher Education, Science and Technology, and the Indonesian Endowment Fund for Education (LPDP). Additionally, this research was also supported by funding from the Department of Civil Engineering, Institut Teknologi Sepuluh Nopember, Surabaya, Indonesia.

6.4. Conflicts of Interest

The authors declare no conflict of interest.

7. References

[1] Abu-Farsakh, M., Dhakal, S., & Chen, Q. (2015). Laboratory characterization of cementitiously treated/stabilized very weak subgrade soil under cyclic loading. Soils and Foundations, 55(3), 504–516. doi:10.1016/j.sandf.2015.04.003.

[2] Ardah, A., Abu-Farsakh, M., & Chen, Q. (2016). Evaluating the Performance of Cementitious Treated/Stabilized Very Weak and Wet Subgrade Soils for Sustainable Pavement. American Society of Civil Engineers: Geo-Chicago 2016, 567–576. doi:10.1061/9780784480137.054.

[3] Antunes, V., Simão, N., & Freire, A. C. (2017). A Soil-Cement Formulation for Road Pavement Base and Sub Base Layers: a Case Study. Transportation Infrastructure Geotechnology, 4(4), 126–141. doi:10.1007/s40515-017-0043-9.

[4] Tan, E. H., & Zahran, E. M. M. (2020). A laboratory investigation of the compaction properties of road sub-base stabilised with cement and latex copolymer. IOP Conference Series: Materials Science and Engineering, 943(1), 012015. doi:10.1088/1757-899X/943/1/012015.

[5] Saurav, S., & Sinha, S. (2025). Evaluation of Cementitiously Stabilized Granular Materials for Low Volume Roads in India. International Journal of Pavement Research and Technology, 18(4), 1065–1082. doi:10.1007/s42947-023-00399-4.

[6] Al-Homidy, A. A., Abd El Aal, A. K., Nabawy, B. S., & Radwan, A. E. (2024). Effect of adding cement kiln dust on the effective geotechnical properties of sand dunes in Najran–Sharourah, Kingdom of Saudi Arabia: a laboratory study. Journal of Material Cycles and Waste Management, 26(1), 373–391. doi:10.1007/s10163-023-01831-4.

[7] Ghandehari, M. A., & Seyedi Hosseininia, E. (2025). A Numerical Investigation on the Mechanical Behavior of Cemented Sand with Angular Particles by Using DEM. Arabian Journal for Science and Engineering, 50(3), 1579–1599. doi:10.1007/s13369-024-08995-7.

[8] Alhakim, G., Baalbaki, O., & Jaber, L. (2022). Effects of incorporation of cement and metakaolin on the mechanical properties of poorly graded sand. Arabian Journal of Geosciences, 15(24), 1777. doi:10.1007/s12517-022-11080-8.

[9] Salunkhe, A., Sre Adethya, V., Gobinath, R., Hari Prasanth, J., & Karthikeyan, S. (2022). Shear behaviour of cement treated sand. Materials Today: Proceedings, 68, 1266–1272. doi:10.1016/j.matpr.2022.06.077.

[10] Boutouba, K., Benessalah, I., Arab, A., & Henni, A. D. (2019). Shear Strength Enhancement of Cemented Reinforced Sand: Role of Cement Content on the Macro-Mechanical Behavior. Studia Geotechnica et Mechanica, 41(4), 200–211. doi:10.2478/sgem-2019-0020.

[11] Wang, Y. H., & Leung, S. C. (2008). A particulate-scale investigation of cemented sand behavior. Canadian Geotechnical Journal, 45(1), 29–44. doi:10.1139/T07-070.

[12] Yang, H., Qian, Z., Yue, B., & Xie, Z. (2024). Effects of Cement Dosage, Curing Time, and Water Dosage on the Strength of Cement-Stabilized Aeolian Sand Based on Macroscopic and Microscopic Tests. Materials, 17(16), 3946. doi:10.3390/ma17163946.

[13] Wang, W., Huang, J., Chen, D., Luo, Q., & Yuan, B. (2025). The Effect of Cementation on Microstructural Evolution and Particle Characteristics of Calcareous Sand Under Triaxial Loading. Buildings, 15(12), 1–20. doi:10.3390/buildings15122041.

[14] Ocheme, J. I., Kim, J., & Moon, S. W. (2024). Enhancing geomechanical characteristics of calcium sulfoaluminate (CSA) cement-treated soil under low confining pressures. Scientific Reports, 14(1), 1–19. doi:10.1038/s41598-024-61548-8.

[15] Javed, I., Ekinci, A., & Akintuğ, B. (2025). Utilization of Artificially Cemented Sand for Porous Pavement Applications and Analysis of Runoff Control. Turkish Journal of Civil Engineering, 36(5), 111–148. doi:10.18400/tjce.1603567.

[16] Al-Adhadh, A. R., Nik Daud, N. N., Yusuf, B., & Al-Rkaby, A. H. (2025). Effect of Fines on the Geotechnical Properties of Cenent Treated Sandy Soils. Tikrit Journal of Engineering Sciences, 32(3), 1–14. doi:10.25130/tjes.32.3.11.

[17] Xu, L., Xu, R., Lin, Q., Feng, G., Yuan, C., & Ding, Z. (2025). Micro-Mechanism of Strength for Cement-Treated Soil Based on the SEM Experiment: Qualitative and Quantitative Analysis. Buildings, 15(13), 1–11. doi:10.3390/buildings15132370.

[18] Miturski, M. (2025). Novel Proposal for Strength Prediction of Cement-Stabilized Soils Considering Porosity, Cement Index, and Curing Time. Applied Sciences (Switzerland), 15(21), 11448. doi:10.3390/app152111448.

[19] Ahmeti, H., & Behrami, R. (2025). Research on the failure behavior of cement- and fiber-reinforced sand under triaxial tensile loads. Studia Geotechnica et Mechanica, 47(3), 27–45. doi:10.2478/sgem-2025-0018.

[20] Ocheme, J. I., Olagunju, S. O., Khamitov, R., Satyanaga, A., Kim, J., & Moon, S. W. (2023). Triaxial shear behavior of calcium sulfoaluminate (CSA)-treated sand under high confining pressures. Geomechanics and Engineering, 33(1), 41–51. doi:10.12989/gae.2023.33.1.041.

[21] Abdulla, A. A., & Kiousis, P. D. (1997). Behavior of cemented sands - I. Testing. International Journal for Numerical and Analytical Methods in Geomechanics, 21(8), 533–547. doi:10.1002/(sici)1096-9853(199708)21:8<533::aid-nag889>3.0.co;2-0.

[22] Amini, Y., & Hamidi, A. (2014). Triaxial shear behavior of a cement-treated sand-gravel mixture. Journal of Rock Mechanics and Geotechnical Engineering, 6(5), 455–465. doi:10.1016/j.jrmge.2014.07.006.

[23] Hou, T. S., & Xu, G. L. (2009). Experiment on triaxial pore water pressure-stress-strain characteristics of foamed particle light weight soil. Zhongguo Gonglu Xuebao/China Journal of Highway and Transport, 22(6), 10–17.

[24] Jiang, J., Xiao, P., & Li, B. (2017). A novel triaxial test system for concrete under passive confinement. Journal of Testing and Evaluation, 46(3), 913–923. doi:10.1520/JTE20160547.

[25] Haimson, B., & Chang, C. (2000). A new true triaxial cell for testing mechanical properties of rock, and its use to determine rock strength and deformability of Westerly granite. International Journal of Rock Mechanics and Mining Sciences, 37(1–2), 285–296. doi:10.1016/s1365-1609(99)00106-9.

[26] Touhari, M., & Mitiche-Kettab, R. (2016). Behaviour of FRP confined concrete cylinders: Experimental investigation and strength model. Periodica Polytechnica Civil Engineering, 60(4), 647–660. doi:10.3311/PPci.8759.

[27] Khaloo, A., Tabatabaeian, M., & Khaloo, H. (2020). The axial and lateral behavior of low strength concrete confined by GFRP wraps: An experimental investigation. Structures, 27(February), 747–766. doi:10.1016/j.istruc.2020.06.008.

[28] Otoom, O. F., Lokuge, W., Karunasena, W., Manalo, A. C., Ozbakkaloglu, T., & Thambiratnam, D. (2021). Experimental and numerical evaluation of the compression behaviour of GFRP-wrapped infill materials. Case Studies in Construction Materials, 15(August), 654. doi:10.1016/j.cscm.2021.e00654.

[29] Piscesa, B., Attard, M. M., Samani, A. K., & Tangaramvong, S. (2017). Plasticity constitutive model for stress-strain relationship of confined concrete. ACI Materials Journal, 114(2), 361–371. doi:10.14359/51689428.

[30] Haeri, S. M., Hosseini, S. M., Toll, D. G., & Yasrebi, S. S. (2005). The behaviour of an artificially cemented sandy gravel. Geotechnical and Geological Engineering, 23(5), 537–560. doi:10.1007/s10706-004-5110-7.

[31] Teng, J. C., Chen, W. B., Song, D. B., Jin, Y. F., Yin, Z. Y., Dai, J. G., & Chen, X. S. (2025). Behaviour of GFRP-confined sand and cemented sand under four-point flexural tests. Acta Geotechnica, 1-17. doi:10.1007/s11440-025-02835-0.

[32] ACI 230.1R-90. (1990). State-of-the-art report on soil-cement. American Concrete Institute, Michigan, United States. doi:10.14359/2140

[33] ACI 440.2R-17. (2017). Guide for the design and construction of externally bonded FRP systems for strengthening concrete structures. American Concrete Institute, Michigan, United States. doi:10.14359/51700867.

[34] ASTM D3039/D3039M-17. (2017). Standard Test Method for Tensile Properties of Polymer Matrix Composite Materials. ASTM International, Pennsylvania, United States. doi:10.1520/D3039_D3039M-17.

[35] Bhat, R., Mohan, N., Sharma, S., Pratap, A., Keni, A. P., & Sodani, D. (2019). Mechanical testing and microstructure characterization of glass fiber reinforced isophthalic polyester composites. Journal of Materials Research and Technology, 8(4), 3653–3661. doi:10.1016/j.jmrt.2019.06.003.

[36] Stanciu, M. D., Drăghicescu, H. T., & Roșca, I. C. (2021). Mechanical properties of GFRPs exposed to tensile, compression and tensile—tensile cyclic tests. Polymers, 13(6), 898. doi:10.3390/polym13060898.

[37] Piscesa, B., Attard, M. M., & Samani, A. K. (2016). A lateral strain plasticity model for FRP confined concrete. Composite Structures, 158, 160–174. doi:10.1016/j.compstruct.2016.09.028.

[38] Orilogi, E., Berry, S. M., & MacLaughlin, M. M. (2020). Evaluating volumetric strain for identifying the loading stage termination points for the multistage triaxial test: A case study with Utah coal specimens. 54th U.S. Rock Mechanics/Geomechanics Symposium. Montana Technological University, Montana, United States.

[39] Lloret-Cabot, M., Wheeler, S. J., & Sánchez, M. (2013). Unification of plastic compression in a coupled mechanical and water retention model for unsaturated soils. Canadian Geotechnical Journal, 51(12), 1488–1493. doi:10.1139/cgj-2013-0360.

[40] Samani, A. K., & Attard, M. M. (2014). Lateral strain model for concrete under compression. ACI Structural Journal, 111(2), 441–451. doi:10.14359/51686532.

[41] Jiang, H. (2015). Failure criteria for cohesive-frictional materials based on Mohr-Coulomb failure function. International Journal for Numerical and Analytical Methods in Geomechanics, 39(13), 1471–1482. doi:10.1002/nag.2366.

[42] Barsanescu, P., Sandovici, A., & Serban, A. (2018). Mohr-Coulomb criterion with circular failure envelope, extended to materials with strength-differential effect. Materials and Design, 148, 49–70. doi:10.1016/j.matdes.2018.03.043.

[43] Labuz, J. F., & Zang, A. (2012). Mohr–Coulomb Failure Criterion. Rock Mechanics and Rock Engineering, 45(6), 975–979. doi:10.1007/s00603-012-0281-7.

[44] Yu, T., Teng, J. G., Wong, Y. L., & Dong, S. L. (2010). Finite element modeling of confined concrete-I: Drucker–Prager type plasticity model. Engineering Structures, 32(3), 665–679. doi:10.1016/j.engstruct.2009.11.014.

[45] Papanikolaou, V. K., & Kappos, A. J. (2007). Confinement-sensitive plasticity constitutive model for concrete in triaxial compression. International Journal of Solids and Structures, 44(21), 7021–7048. doi:10.1016/j.ijsolstr.2007.03.022.

[46] Irmawan, M., Piscesa, B., Alrasyid, H., & Suprobo, P. (2022). Numerical Modeling of Steel Fiber Reinforced Concrete Beam with Notched under Three-point Bending Test. Civil Engineering and Architecture, 10(7), 3227–3242. doi:10.13189/cea.2022.100733.

[47] Chen, J., Wang, W., & Chen, L. (2023). A Strain Hardening and Softening Constitutive Model for Hard Brittle Rocks. Applied Sciences (Switzerland), 13(5), 2764. doi:10.3390/app13052764.